ACS NANO

www.acsnano.org

ARTICLE

Dual-Modal Nanoplasmonic Light Upconversion through Anti-Stokes Photoluminescence and Second-Harmonic Generation from Broadband Multiresonant Metal Nanocavities

Seied Ali Safiabadi Tali,[§] Rathsara R. H. H. Mudiyanselage,[§] Yizhou Qian, Nicholas William Gary Smith, Yuming Zhao, Ada Morral, Junyeob Song, Meitong Nie, Brenden A. Magill, Giti A. Khodaparast,* and Wei Zhou*

Cite This: https://doi.org/10.1021/acsnano.3c00559

ABSTRACT: Metal nanocavities can generate plasmon-enhanced light upconversion signals under ultrashort pulse excitations through anti-Stokes photoluminescence (ASPL) or nonlinear harmonic generation processes, offering various applications in bioimaging, sensing, interfacial science, nanothermometry, and integrated photonics. However, achieving broadband multiresonant enhancement of both ASPL and harmonic generation processes within the same metal nanocavities remains challenging, impeding applications based on dual-modal or wavelength-multiplexed operations. Here, we report a combined experimental and theoretical study on dual-modal plasmon-enhanced light upconversion through both ASPL and second-harmonic generation (SHG) from broadband multiresonant metal nanocavities in two-tier Ag/SiO_2/Ag nanolaminate plasmonic crystals (NLPCs) that can support multiple hybridized plasmons with high spatial mode overlaps. Our measurements reveal the distinctions and correlations between the plasmon-enhanced ASPL and SHG processes under different modal and ultrashort pulsed laser excitation conditions, including incident fluence, wavelength, and polarization. To analyze the observed effects of the excitation and modal conditions on the ASPL and SHG emissions, we developed a time-domain modeling framework that simultaneously captures the mode coupling-enhancement characteristics, quantum excitation−emission transitions, and hot carrier population statistical mechanics. Notably, ASPL and SHG from the same metal nanocavities exhibit distinct plasmon-enhanced emission behaviors due to the intrinsic differences between the incoherent hot carrier-mediated ASPL sources with temporally evolving energy and spatial distributions and instantaneous SHG emitters. Mechanistic understanding of ASPL and SHG emissions from broadband multiresonant plasmonic nanocavities marks a milestone toward creating multimodal or wavelength-multiplexed upconversion nanoplasmonic devices for bioimaging, sensing, interfacial monitoring, and integrated photonics applications.

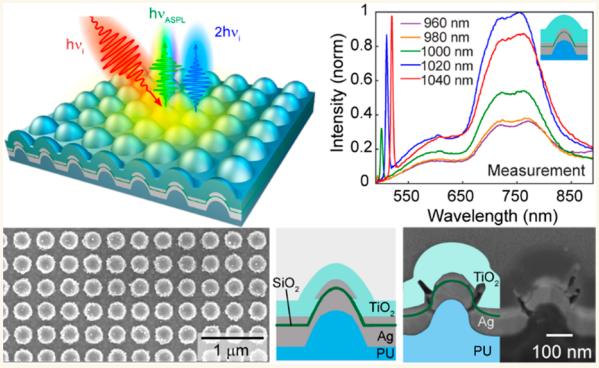

KEYWORDS: *nonlinear plasmonics, broadband multiresonant nanocavity, nanolaminate plasmonic crystals, second-harmonic generation, anti-Stokes photoluminescence, hot electrons and holes, intraband recombination*

INTRODUCTION

Metal nanocavities can support surface plasmon modes, concentrating optical fields in the nanoscale matter to enhance various luminescence processes, including spontaneous and stimulated emission, resonant and nonresonant Raman scattering, and nonlinear harmonic generation.[1−6] Notably,

Received: January 19, 2023
Accepted: May 2, 2023

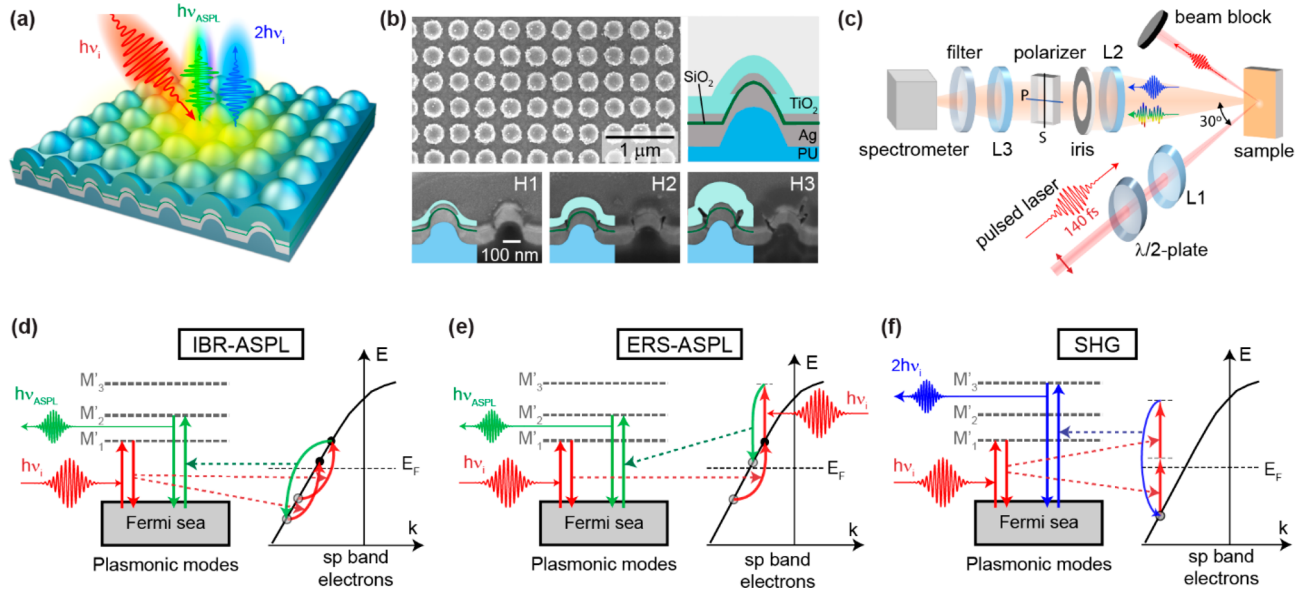

Figure 1. Probing plasmon-enhanced second harmonic generation (SHG) and anti-Stokes photoluminescence (ASPL). (a) A cartoon illustration of the SHG and ASPL emission from nanolaminate plasmonic crystals (NLPCs) upon NIR ultrashort pulsed laser excitation. (b) The top-view and cross-sectional SEM images of the NLPC samples with different TiO_2 capping layer thicknesses (h): H1 (h = 25 nm), H2 (h = 60 nm), and H3 (h = 130 nm). (c) The schematic illustration of the upconversion emission measurement setup. (d–f) Energy diagrams representing the multiresonant plasmon enhancement of the (d) intraband recombination (IBR) mediated ASPL, (e) electronic Raman scattering (ERS) mediated ASPL, and (f) SHG processes.

even without incorporating additional luminescent materials, metal nanocavities can directly generate plasmon-enhanced upconversion luminescence signals under ultrashort pulse excitations through nonlinear harmonic generation[7−13] or anti-Stokes photoluminescence (ASPL).[14−19] Plasmon-enhanced excitation or emission transitions at metallic surfaces with broken centrosymmetry enable metal nanocavities to produce narrowband coherent second harmonic generation (SHG) signals, with applications in bioimaging, sensing, and integrated photonics.[20−25] In contrast, ASPL from metal nanocavities exhibits broadband upconversion emission spectra, which are useful for bioimaging, nanothermometry, and interfacial chemical reaction monitoring.[14,26−31] However, generation mechanisms of nanoplasmonic ASPL remain under debate due to the potential involvement of several plasmon-enhanced pathways, including interband recombination of excited electron−hole pairs between metal sp and d bands,[32,33] intraband recombination (IBR) of excited electron−hole pairs within the metal sp band,[34−37] and instantaneous electronic Raman scattering (ERS) of sp band electrons via intermediate virtual states.[18,19,38−40] Moreover, it is still debated[41] whether ASPL photons originate from plasmon-enhanced radiative electron−hole pair recombination[15,34,36,42] or emitted via the surface plasmons excited by a nonradiative recombination process.[43−45] Furthermore, even with growing research efforts, limited investigation exists regarding the differences and connections between ASPL and harmonic generation processes in the same metal nanocavities, as well as their dependence on optical excitation and modal conditions. This gap impedes the mechanistic understanding of various plasmon-mediated ASPL and harmonic generation pathways and their interrelationships, which is crucial for developing multimodal or wavelength-multiplexed nano-optics devices based on plasmonic light upconversion in broadband multiresonant metal nanocavities.

Here, we report a combined experimental and theoretical study on dual-modal plasmon-enhanced light upconversion through ASPL and SHG from broadband multiresonant metal nanocavities under near-infrared (NIR) ultrashort pulsed laser excitation (Figure 1a). Our study employs the recently developed two-tier $Ag/SiO_2/Ag$ nanolaminate plasmonic crystals (NLPCs)[46] that can support multiple hybridized plasmon modes with high spatial overlap for broadband multiresonant enhancement of multiphoton excitation and emission transitions in ASPL and SHG from metallic hotspots (Figure 1a,b). We have conducted measurements to investigate the differences and correlations between the plasmon-enhanced ASPL and SHG processes under different ultrashort pulsed laser excitation conditions, including incident fluence, wavelength, and polarization. Also, by engineering the NLPCs' plasmonic modes at the excitation and emission wavelengths, we have studied how the plasmonic enhancement of the excitation and emission transitions can affect the ASPL and SHG emission properties.

To understand the observed effects of the optical excitation and modal conditions on the ASPL and SHG emission properties, we developed a time-domain modeling framework combining optical simulations, coupled-mode theory, quantum optics, and hot carrier statistical mechanics. Notably, our plasmon-enhanced ASPL model incorporates both IBR (Figure 1d) and ERS (Figure 1e) pathways, while our plasmon-enhanced SHG model (Figure 1f) accounts for the second-order susceptibility modification due to the electron distribution perturbation. By fitting the measured trends of the ASPL and SHG power laws and spectral features, we find that the IBR can be the dominant ASPL pathway in multiresonant metal nanocavities of NLPCs. Our study further reveals that the relative contribution levels of the native (thermally excited before the excitation), excess nonthermalized, and excess thermalized hot carriers to the IBR-mediated ASPL emission

https://doi.org/10.1021/acsnano.3c00559
ACS Nano XXXX, XXX, XXX−XXX

can significantly influence its input-output power-law, spectral and temporal characteristics. By analyzing the correlations between the excitation laser and the nonlinear emission polarizations, we demonstrate that both ASPL and SHG photons come from radiative surface plasmon decay rather than radiative electronic transitions within the sp band (Figure 1d−f). Furthermore, we find that ASPL and SHG from the same metal nanocavities exhibit different plasmon-enhanced emission behaviors due to the intrinsic differences between the incoherent hot carrier-mediated ASPL sources with time-dependent energy and spatial distributions and instantaneous SHG emitters. We envision that NLPCs can provide a versatile multiresonant nanoplasmonic platform to explore broadband multiresonant enhancement of both ASPL and harmonically generated signals, leading to upconversion nano-optics devices based on multimodal and wavelength-multiplexed operations.

RESULTS AND DISCUSSION

We have employed a combination of nanoimprint lithography and electron beam deposition techniques[47] to create Ag-based conventional plasmonic crystal samples (G1−G3) and NLPC samples (H1−H3) with anticorrosion TiO_2 capping layers of different thicknesses: ≈25 nm for H1/G1, ≈60 nm for H2/G2, and ≈130 nm for H3/G3 (Table 1 and Figure 2a). By design,

Table 1. Description of H1−H3 and G1−G3 Plasmonic Crystal Samples, Where the Metal and Dielectric Layers Are Deposited on a Polymer Nanopillar Array with 400 nm Periodicity

sample	description
H1	Ag (80 nm)/SiO_2 (6 nm)Ag (30 nm)/TiO_2 (25 nm)
H2	Ag (80 nm)/SiO_2 (6 nm)Ag (30 nm)/TiO_2 (60 nm)
H3	Ag (80 nm)/SiO_2 (6 nm)Ag (30 nm)/TiO_2 (130 nm)
G1	Ag (80 nm)/TiO_2 (25 nm)
G2	Ag (80 nm)/TiO_2 (60 nm)
G3	Ag (80 nm)/TiO_2 (130 nm)

G1−G3 samples consist of a single Ag layer (≈80 nm) on top of a polymer nanopillar array (periodicity = 400 nm) to support delocalized Bloch surface plasmon polariton (SPP) modes on the Ag-TiO_2 interface. H1−H3 samples (Figure 1b) include additional nanolaminated SiO_2 (≈6 nm) and Ag (≈30 nm) layers to support gap Bloch SPP modes inside their periodically corrugated Ag/SiO_2/Ag metal−insulator−metal (MIM) nanosandwich, in addition to the delocalized modes on the Ag-TiO_2 interface. Furthermore, Ag/SiO_2/Ag nanodomes on top of the nanopillars in H1−H3 can support multiple localized MIM gap plasmons to hybridize with their delocalized modes through near-field optical coupling.

We employed spectrophotometry to measure the reflectance spectra (Figure 2b) of the H1−H3 and G1−G3 samples and compared these results with the reflectance spectra derived from finite-difference time-domain (FDTD) calculations (Figure 2c). Generally, the FDTD-calculated reflectance spectra exhibit good agreement with the measurements. Due to the 80 nm Ag layer, all the samples have negligible transmittance, and thus the reflectance dips can represent the resonant absorption peaks of the different modes ($R \approx 1 - A$). To better understand the microscopic characteristics of different plasmonic modes in the samples, we plot the corresponding near-field mode profiles of resonant features for H3 and G3 samples in Figures 2d-e. There are several crucial observations. First, H1−H3 and G1-G3 samples exhibit similar resonant reflectance dips below 950 nm. As revealed in the near-field profiles, the modes below 950 nm, including the λ_1, λ_2, and λ_3 resonances for H3 and λ'_1, λ'_2, and λ'_3 resonances for G3, are primarily associated with Bloch SPP modes of different grating orders on the Ag-TiO_2 interface. Both λ_1−λ_3 modes in H3 and λ'_1− λ'_3 modes in G3 can concentrate the optical fields on the outer surface of the nanodomes with $|E|^2$ enhancement factors of 10^1 to 10^2 (Figure 2d-e). Second, in both H1−H3 and G1-G3 samples, the resonances below 950 nm redshift with increasing TiO_2 capping layer thicknesses due to a higher effective dielectric refractive index at the Ag-TiO_2 interface. Third, G1−G3 samples have negligible optical absorption above 950 nm. Only G3 shows a broad Bloch SPP resonance around λ'_4 = 1400 nm. In contrast, H1−H3 samples show multiple resonant reflectance dips above 950 nm, almost unaffected by the TiO_2 capping layer thickness. Near-field profiles in Figure 2d reveal that λ_4 and λ_5 resonances originate from the gap Bloch SPP modes in Ag/SiO_2/Ag layers, while λ_6 resonance is due to the localized gap plasmons in the Ag/SiO_2/Ag nanodomes. Finally, all the λ_1−λ_6 near-field mode profiles (Figure 2d) show intensely concentrated optical fields inside the Ag/SiO_2/Ag nanodomes with $|E|^2$ enhancement factors of 10^2 to 10^3, suggesting high spatial mode overlaps due to effective optical hybridization between the localized gap plasmonic modes in the Ag/SiO_2/Ag nanodomes and the delocalized modes on the Ag-TiO_2 interface and in the Ag/SiO_2/Ag nanosandwich.

To investigate the nonlinear optical responses of the samples, we conducted free-space upconversion emission measurements (Figure 1c) under ultrashort pulsed laser excitation (Δt_{inc} = 140 fs pulse duration and f_{inc} = 80 MHz repetition rate) at 30° incident angle and with emission collection in the 490−890 nm spectral range at the normal angle. With pulsed laser excitation at incident wavelengths $\lambda_{inc} \geq 960$ nm, G1−G3 samples can only enhance the nonlinear emission transitions, while H1−H3 samples can simultaneously enhance both the excitation and emission transitions due to their broadband multiresonance with spatial mode overlap. Figure 3a shows the upconversion emission spectra of H1/G1, H2/G2, and H3/G3 samples under P-polarized excitation at the incident wavelength of λ_{inc} = 1020 nm and the incident fluence of E_{inc} = 204 nJ/cm^2. There are several important observations. First, both G1-G3 and H1−H3 samples feature a sharp SHG peak at 510 nm together with a broad ASPL emission that quickly drops below the SHG wavelength. Compared to G1-G3 samples without MIM nanogaps, H1−H3 samples produce one to two orders higher SHG and ASPL emission intensities due to the absorption enhancement by the MIM gap plasmons at the pump wavelength of 1020 nm. Furthermore, we find a spectral correlation between the ASPL emission peaks and the reflectance dips (or absorption peaks) in both H1−H3 and G1−G3 samples (SI, Figure S1), revealing that the plasmonic modes across the ASPL spectral band enhance the emission process through the Purcell effect.[15]

In Figure 3b, the measured upconversion emission spectra from the H3 sample at different incident fluence levels (E_{inc}) show that the SHG and ASPL signals increase nonlinearly with the fluence (corresponding power and irradiance levels in Table S1). Interestingly, the ASPL spectral lineshapes (Figure 3c) barely change with the increased fluence up to $E_{inc} \sim 127$ nJ/cm^2, and only slight spectral blueshifts occur at higher fluence levels ($E_{inc} \geq 178$ nJ/cm^2). Also, the ASPL emission below the SHG wavelength at 510 nm is negligible for the fluence levels

https://doi.org/10.1021/acsnano.3c00559
ACS Nano XXXX, XXX, XXX−XXX

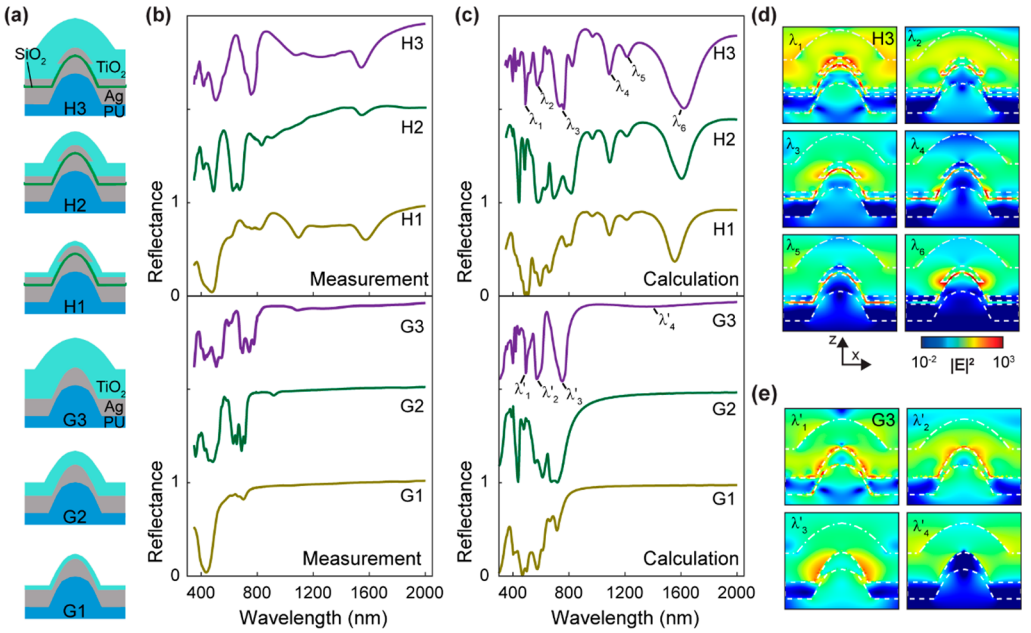

Figure 2. Passive optical properties of the designed samples. (a) Schematic illustration of the H1−H3 and G1−G3 samples. (b-c) The measured and FDTD-calculated reflectance spectra of the samples. (d-e) FDTD-calculated near-field $|E|^2$ profiles of the H3 and G3 samples at the resonances marked in their reflectance spectra.

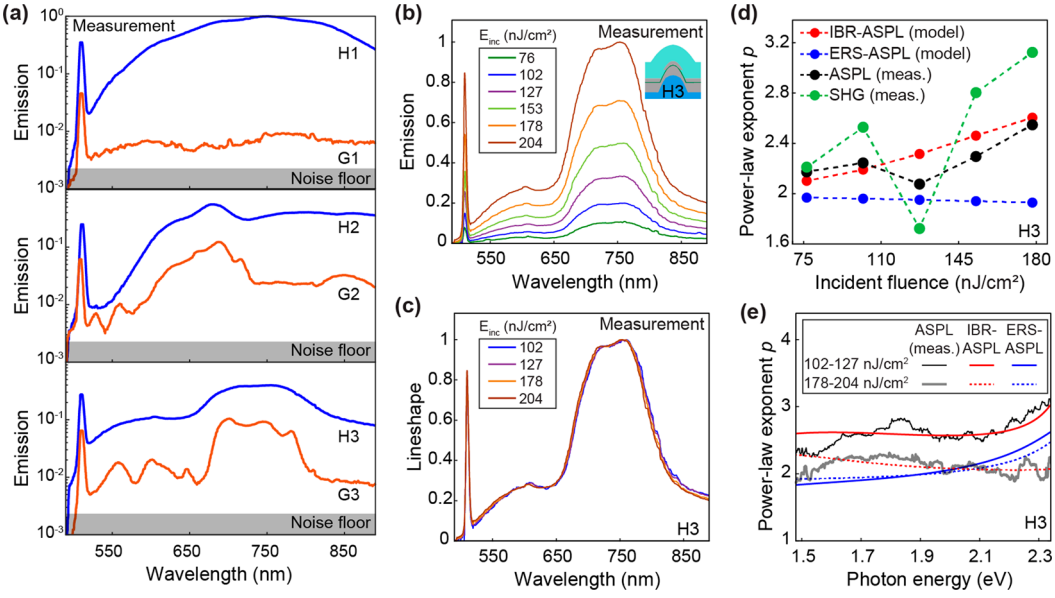

Figure 3. Influence of design geometry and fluence on the upconversion emission spectra. (a) The measured upconversion emission spectra of the H1/G1, H2/G2, and H3/G3 samples under ultrashort pulsed laser excitation (P-polarized, λ_{inc} = 1020 nm, and E_{inc} = 204 nJ/cm²). H and G samples in each graph share the same TiO_2 capping layer thickness. (b) The measured upconversion emission spectra and (c) lineshapes from the H3 sample under ultrashort pulsed laser excitation (P-polarized, λ_{inc} = 1020 nm) at different fluence levels (E_{inc} = 76 nJ/cm² up to E_{inc} = 204 nJ/cm²). (d) The fluence-dependent spectrally integrated power-law exponents (p) from the measured SHG (505−515 nm) and ASPL (530−890 nm) signals, and simulations based on the IBR-ASPL and ERS-ASPL models. (e) The spectrally resolved power-law exponents (p) from the measured ASPL spectra and simulations based on the IBR-ASPL and ERS-ASPL models at two different fluence ranges.

less than E_{inc} ~ 204 nJ/cm² (Figure S2 in SI). By exponential fitting, we find that the SHG signals (integrated from 505 to 515 nm) and the ASPL signals (integrated from 530 to 890 nm) have power-law exponents of ≈2.36 and ≈2.22 across all the input fluence levels (Figure S3b in SI), suggesting that the two-photon excitation processes dominantly contribute to the nonlinear emission signals. However, as shown in Figure 3d, the differential power-law exponents of the SHG and ASPL signals (SI, section 1) vary with the fluence due to the contribution of higher-order processes to the plasmon-enhanced SHG and ASPL emissions. Both the SHG and ASPL power-law exponents increase with E_{inc} from 76 to 102 nJ/cm² and from 127 to 178 nJ/cm² but show an anomalous decrease around E_{inc} = 127 nJ/cm², especially for SHG. We hypothesize that the observed anomalies in the fluence-dependent SHG and ASPL power-law exponents may be associated with the subtle reversible geometric modifications (e.g., local thermal expansion) and the uneven lattice temperature induced by the plasmonic

https://doi.org/10.1021/acsnano.3c00559
ACS Nano XXXX, XXX, XXX−XXX

photothermal effects at the metal interface. The SHG power-law anomaly could also result from the alteration of the second-order susceptibility $\chi^{(2)}$ due to plasmon-enhanced hot carrier generation and the subsequent changes in electron distribution at the metal surface.[48,49] Further investigation is required to fully understand the observed power-law anomalies.

By spectral analysis of the fluence-dependent ASPL power-law exponents[16] in Figure 3e and Figure S3d in SI, we find that the power-law exponent can vary with the emission photon energy ($h\nu$) but remains ≈2 for $E_{inc} \leq 127$ nJ/cm^2. As E_{inc} increases above 127 nJ/cm^2, the power-law exponent grows above 2 and gradually assumes an increasing trend with $h\nu$, consistent with the slight blueshift observed in the ASPL emission spectral shape in Figure 3c. In what follows, we will show that the observed fluence-dependent behaviors of the ASPL emission result from an IBR-dominant PL process.

Before the ultrashort pulsed laser excitation, the electrons in the metal are at thermal equilibrium with the lattice and follow the Fermi−Dirac distribution $\rho_0(\epsilon) = f(\epsilon, T_0) = \frac{1}{\left[\exp\left(\frac{\epsilon - E_F}{K_B T_0}\right) + 1\right]}$, where ϵ is the electron energy, E_F = 5.49 eV is the silver Fermi energy, K_B denotes the Boltzmann constant, and T_0 = 300 K is the room temperature. The system only contains a small concentration of thermally excited native hot carriers (i.e., hot electrons and hot holes) in the pre-excitation state. Absorption of ultrashort laser pulse photons can abruptly generate excess hot carriers to perturb the equilibrium electron distribution in the energy range from $\sim E_F - h\nu_{inc}$ up to $\sim E_F + h\nu_{inc}$, where h is Planck's constant and ν_{inc} is the incident laser frequency. The incident laser pulse also resonantly excites the surface plasmons that enhance the light absorption and hot carrier generation through the Landau damping process.[50] The time-dependent hot carrier generation rate, $G_{inc}(\epsilon,t)$, can be expressed to the first order as[51,52]

$$G_{inc}(\epsilon, t) = \frac{M_{inc} I_{inc}(t)}{\sqrt{\epsilon}} \{\sqrt{\epsilon - h\nu_{inc}} f(\epsilon - h\nu_{inc}, T_0)[1 - f(\epsilon, T_0)] - \sqrt{\epsilon + h\nu_{inc}} f(\epsilon, T_0)[1 - f(\epsilon + h\nu_{inc}, T_0)]\} \quad (1)$$

where M_{inc} (m^2/J) accounts for the local excitation strength and depends on the system modal characteristics and excitation conditions such as wavelength and polarization. $I_{inc}(t) = \frac{0.88 E_{inc}}{\Delta t_{inc}}\left[\mathrm{sech}\left(\frac{1.76t}{\Delta t_{inc}}\right)\right]^2$ is the instantaneous incident irradiance, where Δt_{inc} = 140 fs and E_{inc} are the temporal width and fluence of the laser pulse, respectively, and "sech" represents the hyperbolic secant function.

A common perturbation-based approach is to divide the total electron distribution as $\rho(\epsilon,t) = \rho_{nt}(\epsilon,t) + \rho_t(\epsilon,t)$, where the nonthermalized component ρ_{nt} has a non-Fermi distribution, and the thermalized component ρ_t has a Fermi−Dirac distribution at the electronic temperature $T_e(t) \geq T_0$.[53] In the equilibrium condition before the excitation ($t = -\infty$), $T_e = T_0$ and $\rho_{nt} = 0$. The excitation process (eq 1) initially generates nonthermalized carriers ($G_{inc} = \frac{d\rho_{nt}}{dt}|_{gen}$) but as soon as the generation occurs, electron−electron (e−e) collisions transfer the energy from the nonthermalized carriers to the thermalized ones, leading to a rise in T_e. Simultaneously, electron−phonon (e−ph) collisions transfer the energy stored in the excess hot carriers to the lattice, and thus eventually, both the non-thermalized and thermalized electron populations decay to their pre-excitation levels. The photoluminescence process also consumes the hot carriers but has a negligible effect on the hot carrier concentration due to its low quantum yield (<10^{-5}).[37] We model the above-described time-evolution of ρ_t and ρ_{nt} using two master equations (SI, Section 2) rigorously built on the charge and energy conservation laws instead of assuming a fixed effective electronic temperature[17] or using a temperature-dependent electronic heat capacity.[19] Given M_{inc}, λ_{inc}, and E_{inc}, we can employ the master equations to model the time evolution of the electron distribution upon the ultrashort pulsed laser excitation. As an example, Figure S4 (in SI) shows $\rho_{nt}(\epsilon,t)$, $\rho_t(\epsilon,t)$, and $\rho(\epsilon,t) = \rho_{nt}(\epsilon,t) + \rho_t(\epsilon,t)$ curves for a system with $M_{inc} = 2 \times 10^{-3}$ cm^2/nJ and excited by a λ_{inc} = 1020 nm and E_{inc} = 204 nJ/cm^2 laser pulse.

We next use the obtained time-dependent electron distributions to calculate the ASPL emission rate. ASPL emission results from electronic transitions across the sp band states induced via the perturbation of the metal intrinsic Hamiltonian (H_0) by the incident field and all the excited and unexcited optical modes: $H_0 \rightarrow H_0 + H_{int}$, where H_{int} is the interaction Hamiltonian.[54] We neglect the interband transitions since both the pump and ASPL emission photon energies (1.22 eV ≤ $h\nu$ ≤ 2.44 eV) are much lower than the ∼4 eV energy separation between d band and the Fermi energy level in silver. After expanding H_{int} with the Coulomb gauge in Maxwell's equations and using Fermi's golden rule, we can express ASPL spectral intensity as (see SI, Section 3):

$$S_{ASPL}(\nu) \propto f_{inc}\left(\frac{4h\nu^3}{c^3}\right) L_{eff}(\nu)[\beta\psi_{IBR}(\nu) + (1 - \beta)\psi_{ERS}(\nu)] \quad (2)$$

where $L_{eff}(\nu)$ is the effective emission enhancement factor that equals the quantum yield enhancement factor for the intrinsically low-yield metallic PL processes,[1] β is a ratio factor between 0 and 1 determining the relative contribution of the IBR or ERS pathways to the ASPL emission, and $\psi_{IBR}(\nu)$ and $\psi_{ERS}(\nu)$ represent the number of electron−hole pairs available for ASPL at frequency ν via the IBR and ERS processes, respectively. $\psi_{IBR}(\nu)$ and $\psi_{ERS}(\nu)$ can be expressed as follows (SI section 3):

$$\psi_{IBR}(\nu) = \int_{-\infty}^{+\infty} \int_{h\nu}^{+\infty} \xi_{IBR}(\epsilon, \nu)\rho(\epsilon, t)[1 - \rho(\epsilon - h\nu, t)] \epsilon^{3/2} d\epsilon dt \quad (3)$$

$$\psi_{ERS}(\nu) = \int_{-\infty}^{+\infty} \left(\frac{I_{inc}(t)}{\nu_{inc}}\right) \int_{h\nu}^{+\infty} \xi_{ERS}(\epsilon, \nu)\rho(\epsilon, t) [1 - \rho(\epsilon + h\nu_{inc} - h\nu, t)]\sqrt{\epsilon d\epsilon dt} \quad (4)$$

where $\xi_{IBR}(\epsilon, \nu) = a(\epsilon)e^{-h\nu/b(\epsilon)KT}$ and $\xi_{ERS}(\epsilon, \nu) = a'(\epsilon)e^{-h(\nu - \nu_{inc})/b'(\epsilon)KT}$ account for the momentum provided by the plasmonic modes in electronic transitions, and $a \approx 32.2$, $b \approx 11.6$, $a' \approx 23.4$, and $b' \approx 23$ are good approximations for our modeling in this work. In the IBR-ASPL process (Figure 1d), the emission of a photon with the energy $h\nu$ requires the recombination of an electron in the state ϵ with the hole in the state $\epsilon - h\nu$ (i.e., an inverse Landau damping process). However, to generate a similar photon in the ERS-ASPL process (Figure 1e), absorption of an incident photon or annihilation of a surface plasmon quasiparticle at the fundamental frequency

https://doi.org/10.1021/acsnano.3c00559
ACS Nano XXXX, XXX, XXX−XXX

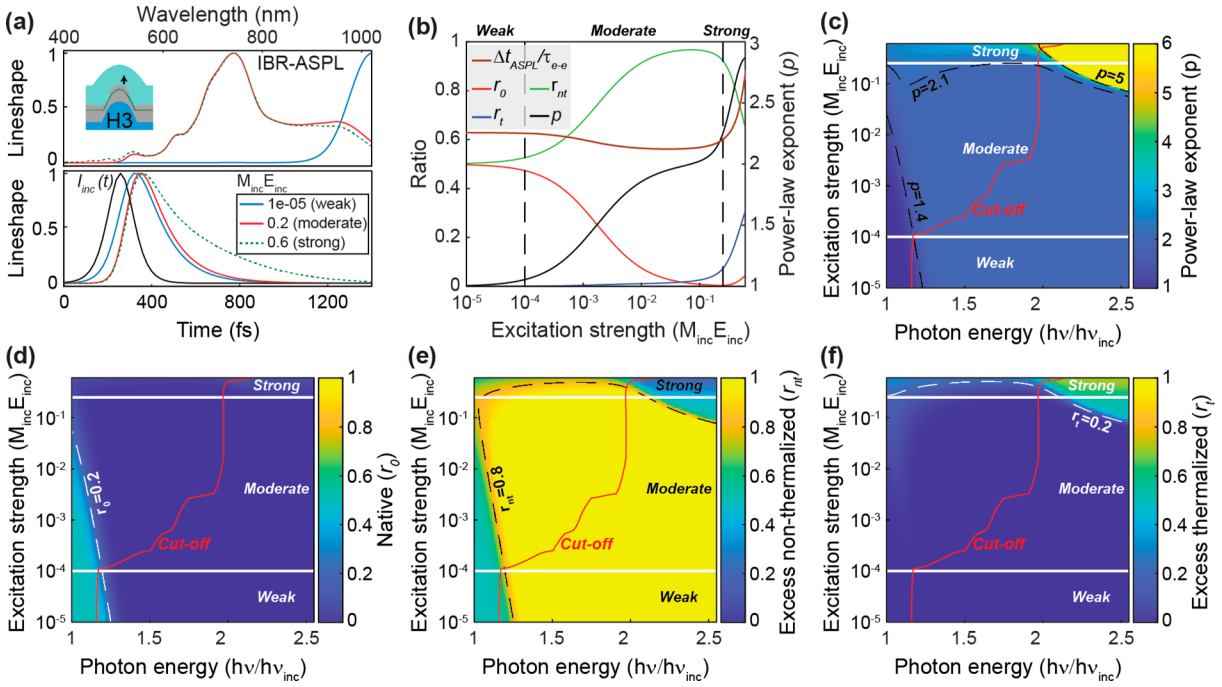

Figure 4. Simulated influences of the excitation strength on the temporal, spectral, and power-law characteristics of the IBR-ASPL emission from the H3 sample under ultrafast pulsed laser excitation (Δt_{inc} = 140 fs and λ_{inc} = 1020 nm). (a) Typical spectral (top panel) and temporal (bottom panel) lineshapes of the ASPL emission at weak ($M_{inc}\,E_{inc} \leq 10^{-4}$), moderate ($10^{-4} < M_{inc}\,E_{inc} \leq 0.25$), and strong ($M_{inc}\,E_{inc} > 0.25$) excitation regimes. The black curve in the bottom panel displays the temporal line shape of the incident laser pulse. (b) The excitation strength dependency of the emission power-law exponent (p), emission duration (Δt_{ASPL}), and the relative contribution ratios of the native (r_0), excess nonthermalized (r_{nt}), and excess thermalized (r_t) carriers to the emission. Power-law exponent (p) is calculated across the whole upconversion spectral range, and τ_{e-e} = 350 fs is the electron thermalization time constant in silver. Two-dimensional maps illustrating the dependences of our: (c) spectral power-law exponent, and (d-f) relative contribution ratios for (d) native, (e) excess nonthermalized, and (f) excess thermalized carriers on the emission photon energy and excitation strength. The red line represents the normalized cutoff photon energy of the ASPL emission.

first excites the electron in the state ϵ to the virtual state $\epsilon + h\nu_{inc}$. Then, the electron in the virtual state recombines with the hole in the state $\epsilon + h\nu_{inc} - h\nu$. As illustrated in eqs 3−4, once the laser excitation pulse intensity I_{inc} (t) decays, ERS-ASPL emission stops while the IBR-ASPL emission can continue. However, as the electronic temperature T_e decreases to the ambient temperature T_0, the IBR-ASPL emission spectrum gradually redshifts toward the blackbody radiation spectrum at T_0.

In eq 2, $L_{eff}(\nu)$ determines the PL resonance features and accounts for both the Purcell effect and quantum efficiency of the plasmonic modes. In the modeling, we estimated $L_{eff}(\nu)$ from FDTD simulations using electric dipole sources (please see SI, sections 3 and 4). For a z-oriented dipole above the silver dome, the FDTD-calculated spectra decently mimic the resonances in the experimental line shapes (Figure 4a and SI, Figures S2 and S5), revealing that the ASPL is prevailed by the dipole-like z-oriented hot electron−hole pairs inside the metallic dome likely due to the combined effects of higher generation rate and larger Purcell factor. Hence, the only unknowns in eqs 1−4, and the two master equations (SI, Section 2) are M_{inc} and β. By fitting the measured ASPL power law exponents, we found $M_{inc} = 2 \times 10^{-3}$ cm^2/nJ and $\beta = 1$, revealing that the IBR process dominates the ASPL emission (Figure 3d-e and SI, Figure S3). Using the fitted M_{inc} and β values, other model predictions can also decently match the experimental observations (SI, Figure S2e-f): (i) IBR-ASPL line shapes weakly depend on the incident power and sharply drop below the SHG wavelength; (ii) Above $E_{inc} \approx 127$ nJ/cm^2, the IBR-ASPL line shape starts to blueshift and rise below the SHG wavelength. In contrast, several predictions of an ERS-dominant model ($\beta = 0$) contradict the experimental observations (Figures 3d,e and SI Figures S2 and S3): (i) The spectrally integrated power-law exponents from the ERS-ASPL model have minor sensitivity to the incident fluence and cannot exceed ≈2 (Figure 3d); (ii) The ERS-ASPL spectral power-law exponents below ≈1.9 eV go down as the incident fluence increases (Figure 3e and SI, Figure S 3f); (iii) ERS-ASPL model can generate emission below the SHG wavelength (Figure S 2d).

As shown in Figure 3, both the ASPL's power-law exponents and spectral features are dependent on the incident fluence, suggesting that various mechanisms might dominate the ASPL emission at different excitation strength levels. Excitation strength is generally influenced by both the incident fluence and plasmonic absorption enhancement at the fundamental wavelength λ_{inc}, and can be characterized by the unitless factor $M_{inc}\,E_{inc}$, based on eq 1. To better understand the underlying ASPL mechanisms, we calculated the ASPL emission's spectral profiles (Figure 4a top panel) and power-law exponents at different excitation strength levels (Figures 4b-c). Here, the spectrally integrated power law exponent (Figure 4b) spans the whole upconversion range ($\nu \geq \nu_{inc}$) and the ASPL cutoff frequency ν_c (Figure 4c) is the frequency where the ASPL intensity drops 20 dB below its peak value. By dropping the temporal integrations in eqs 2−4, we also analyzed the ASPL emission in the time domain (Figure 4a bottom panel) and calculated the emission duration (Δt_{ASPL} = fwhm of the emitted ASPL pulse) at the different excitation strength levels (Figure 4b).

https://doi.org/10.1021/acsnano.3c00559
ACS Nano XXXX, XXX, XXX−XXX

We find that depending on the excitation strength, the ASPL process can generally be categorized into weak ($M_{inc}\,E_{inc} \leq 10^{-4}$), moderate ($10^{-4} < M_{inc}\,E_{inc} \leq 0.25$), or strong ($M_{inc}\,E_{inc} > 0.25$) excitation regimes (Figure 4a-c), each exhibiting distinct temporal, spectral, and power-law features. In Figure 4a, $M_{inc}\,E_{inc} = 10^{-5}$ curves represent the ASPL's typical spectral and temporal line shape characteristics in the weak excitation regime. In this regime, the ASPL emission cutoff frequency is about $\nu_c = 1.16\nu_{inc}$ (Figure 4c), the ASPL duration is about Δt_{ASPL} = 220 fs ($0.63\tau_{e-e}$), and the spectrally integrated power-law exponent remains close to p = 1 across the whole regime (Figure 4b). However, the spectral power law exponent (Figure 4c and SI, S6) is composed of a p = 1 flat region at lower photon energies, which sharply transitions into a p = 2 flat region at $h\nu \approx h\nu_{inc}(1-\log(M_{inc}\,E_{inc})/18)$. Weak excitation of the H3 sample requires $E_{inc} < 5 \times 10^{-2}$ nJ/cm^2, which was not easy to test due to the low signal-to-noise ratio. Nevertheless, the predicted power law and spectral features for the weak regime are consistent with the experimental observations for continuous-wave excitation,[15] as in both cases, the electronic temperature remains close to the lattice temperature ($T_e \approx T_0$).

In Figure 4a, $M_{inc}\,E_{inc}$ = 0.2 curves depict the ASPL's typical spectral and temporal line shape characteristics in the moderate excitation regime. In the moderate regime, the ASPL emission cutoff frequency shifts from $\nu_c = 1.35\nu_{inc}$ at $M_{inc}\,E_{inc} = 10^{-4}$ to $\nu_c = 2\nu_{inc} = \nu_{SHG}$ at $M_{inc}\,E_{inc} = 5 \times 10^{-3}$, remaining constant at $\nu_c = 2\nu_{inc}$ afterward (Figure 4c). The spectrally integrated power-law exponent also gradually increases from $p \approx 1$ at $M_{inc}\,E_{inc} = 10^{-4}$ to $p \approx 2.25$ at $M_{inc}\,E_{inc}$ = 0.25, while Δt_{ASPL} decreases from 220 fs ($0.63\tau_{e-e}$) at $M_{inc}\,E_{inc} = 10^{-4}$ to 195 fs ($0.56\tau_{e-e}$) at $M_{inc}\,E_{inc}$ = 0.03 and then rises to ~210 fs ($0.6\tau_{e-e}$) at $M_{inc}\,E_{inc}$ = 0.25 (Figure 4b). The spectral power law exponent gradually transitions into a nearly flat $p \sim 2$ region with a mild broad peak below the cutoff photon energy $h\nu_c$ while increases steeply at higher photon energies above the cutoff (Figure 4c and SI, S6). A similar broad peak is also observed in the measured spectral power law exponents of the H3 sample in Figure 3e and Figure S3 in SI.

$M_{inc}\,E_{inc}$ = 0.6 curves in Figure 4a represent the ASPL's typical spectral and temporal lineshapes in the strong excitation regime. As the excitation strength $M_{inc}\,E_{inc}$ increases in this regime, the ASPL cutoff frequency surpasses the SHG frequency $\nu_{SHG} = 2\nu_{inc}$ (Figure 4c), and the spectrally integrated power law and Δt_{ASPL} quickly increase toward p = 3 and ~300 fs ($0.85\tau_{e-e}$) at $M_{inc}\,E_{inc}$ = 0.6, respectively (Figure 4b). The spectral power law exponent also goes up (especially at higher photon energies) and gradually transforms into an increasing function of the photon energy $h\nu$, with a steep slope around $h\nu_{SHG} = 2\,h\nu_{inc}$ (Figure 4c and SI, Figure S6). These results align with the experimentally observed features of the H3 sample for $E_{inc} > 127$ nJ/cm^2 (Figure 3 and SI, Figures S2 and S3). Our model's predictions in the moderate and strong excitation regimes also agree with the experimental observations in other studies.[16,17]

By decomposing $\rho(\epsilon,t) = \rho_0(\epsilon) + \rho_{nt}(\epsilon,t) + [\rho_t(\epsilon,t) - \rho_0(\epsilon)]$ in eqs 2−4 (SI section 3), we can infer that the ASPL power-law, spectral, and temporal characteristics depend on the relative contribution ratios of the native (ρ_0 distribution), excess nonthermalized (ρ_{nt} distribution), and excess thermalized ($\rho_t - \rho_0$ distribution) hot carriers to the emission (r_0, r_{nt}, and r_t, respectively). The thermally generated native carriers have a constant population independent of the laser excitation. Excess nonthermalized carriers are generated by the laser pulse (1 incident photon per carrier), and their population decays due to both electron−electron and electron−phonon scattering events, with the time constant of $1/\left(\frac{1}{\tau_{e-e}} + \frac{1}{\tau_{e-ph}}\right) \approx 250$ fs.[52] On the other hand, excess thermalized carriers arise from the equilibration of the $\rho_{nt}(\epsilon,t)$ population due to electron−electron scattering events with the time constant of $\tau_{e-e} \approx 350$ fs[52] and could indirectly consume multiple incident photons, depending on the electronic temperature and carrier energy. Moreover, population of the excess thermalized carriers decays solely due to the electron−phonon scattering events, with the time constant of $\tau_{e-}\,_{ph}$) = 850 fs.[52]

Calculating the spectral and spectrally integrated r_0, r_{nt}, and r_t at different excitation levels (Figure 4b,d−f) reveals the strong correlation between these parameters and the ASPL's power-law, spectral, and temporal features (Figure 4a−c). Notably, the emission is almost equally contributed by the native and excess nonthermalized carriers ($r_0 \approx r_{nt} \approx 0.5$) in the weak-excitation areas with p = 1. In the moderate-excitation areas with $p \sim 2$, excess nonthermalized carriers become the dominant contributor to the emission ($r_{nt} \gg r_0, r_t$). Emission duration (Δt_{ASPL}) remains close to $1/\left(\frac{1}{\tau_{e-e}} + \frac{1}{\tau_{e-ph}}\right)$, the excess nonthermalized carrier lifetime, throughout the weak and moderate excitation regimes. Upon entering the strong-excitation regime ($p > 2$), heightened electronic temperatures diminish r_{nt} while raising r_t, leading to a dramatic increase in both the power law exponent (p) and emission duration (Δt_{ASPL}) (Figure 4b).

Figure 5a shows the H3 nonlinear emission spectra under P-polarized ultrashort pulsed laser excitation with different incident wavelengths λ_{inc} from 960 nm to 1040 nm and a constant fluence of E_{inc} = 204 nJ/cm^2. We find that changing the excitation wavelength λ_{inc} not only affects the ASPL and SHG intensities but also their ratio. Notably, I_{SHG} (integrated between $\frac{\lambda_{inc}}{2} \pm 5$ nm) increases as λ_{inc} increases from 1000 to 1040 nm while I_{ASPL} (integrated in 530−890 nm) becomes the highest for λ_{inc} = 1020 nm (Figure 5b). Moreover, I_{SHG} is ~2 times more sensitive to λ_{inc} change than I_{ASPL}. The high sensitivity of I_{SHG} to the λ_{inc} change can come from (i) λ_{inc}-dependent modification of plasmonic enhancement in both the excitation and emission transitions, and (ii) spectrally dispersive $\chi^{(2)}$at the metal surface.

ASPL emission manifests a more complex behavior as changing λ_{inc} nonuniformly affects the spectral ASPL intensity across the emission band, as revealed by the spectral intensity ratios, $R(\lambda_{inc}, \lambda) = \frac{S(\lambda_{inc},\lambda)}{S(1040\text{ nm},\lambda)}$, in Figure 5c. Furthermore, as indicated by the distinct resonance features in the $R(\lambda_{inc},\lambda)$ spectra for each λ_{inc} value (e.g., 960, 980, 1000, and 1020 nm), changing the incident wavelength not only alters the ASPL intensity but also modifies its spectral line shape (SI, Figure S7). A primary reason for the modification of the ASPL intensity and line shape is the λ_{inc}-dependency of the number of available electron−hole pairs ($\psi_{IBR}(\nu)$) in eq 3. $\psi_{IBR}(\nu)$ is a function of the electron distribution $\rho(\epsilon,t)$ and from eq 1, changing λ_{inc} can modify $\rho(\epsilon,t)$ by changing the incident photon energy ($h\nu_{inc}$) and the excitation strength factor M_{inc} (Figure 5d inset). We previously found $M_{inc}(\lambda_{inc} = 1020\text{ nm}) = 2 \times 10^{-3}$ cm^2/nJ by fitting the experimental power law exponents in Figure 3. We can estimate M_{inc} values for the other incident wavelengths (Figure 5b) from the H3 sample's linear absorption spectrum (SI, section 3).

Utilizing the IBR-ASPL model, we calculated $R_\psi(\lambda_{inc},\lambda)$, the spectral intensity ratios due to λ_{inc}-dependency of ψ_{IBR} (Figure 5d), and found that the $R_\psi(\lambda_{inc},\lambda)$ spectra can capture the general

https://doi.org/10.1021/acsnano.3c00559
ACS Nano XXXX, XXX, XXX−XXX

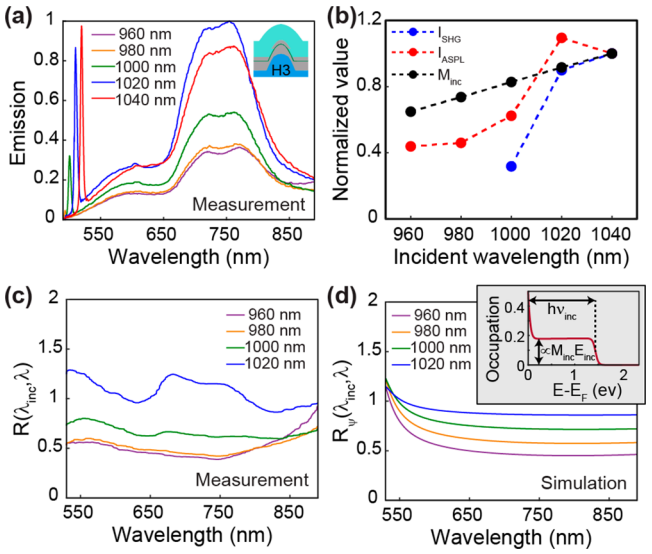

Figure 5. Dependency of the SHG and ASPL emissions on the laser excitation wavelength λ_{inc}. (a) Measured upconversion emission spectra $S(\lambda_{inc},\lambda)$ of the H3 sample under ultrashort pulsed laser excitation (P-polarized and E_{inc} = 204 nJ/cm^2) at different incident wavelengths λ_{inc}. (b) λ_{inc}-dependency of the SHG intensity I_{SHG} (505−515 nm), ASPL intensity I_{ASPL} (530−890 nm), and the excitation strength factor M_{inc} (see eq 1). (c) The ratiometric ASPL spectra, $R(\lambda_{inc}, \lambda) = \frac{S(\lambda_{inc},\lambda)}{S(1040\text{ nm},\lambda)}$, from the measurements at different incident wavelengths in Figure 5a. (d) The simulated ratiometric ASPL spectra, $R_\psi(\lambda_{inc},\lambda)$, when we only consider the effects of λ_{inc} on the electron energy distribution. The inset: Simplified representation of the laser-induced perturbation of the electron energy distribution when the electron−electron and electron−phonon scattering effects are neglected. $h\nu_{inc}$ and M_{inc} E_{inc} determine the perturbation energy range and strength, respectively.

experimental trend that $R(\lambda_{inc},\lambda)$ increases with λ_{inc}. However, R_ψ spectra do not show the resonant features in $R(\lambda_{inc},\lambda)$ curves, indicating that the resonant features are not due to modified $\psi_{IBR}(\nu)$ but originate from a λ_{inc}-dependent effective emission enhancement factor $L_{eff}(\nu)$. Considering the incoherent nature of the IBR-ASPL process, $L_{eff}(\nu)$ can be expressed as (SI, section 4):

$$L_{eff}(\nu) = \sum_{\hat{l}=\hat{x},\hat{y},\hat{z}} \iiint_{V_m} \phi^{\hat{l}}_{eff}(r,\nu) F_{\hat{l}}(r,\nu) d^3r \quad (5)$$

where V_m denotes the metallic parts of the system, and $F_{\hat{l}}(r,\nu)$ represents the radiative decay enhancement of an $\hat{l}$-oriented dipole at position r and frequency ν versus a similar dipole in free space.[54] FDTD simulations show that $F_{\hat{l}}(r,\nu)$ spectrum is very sensitive to r and $\hat{l}$ (SI, Figure S5). $\phi^{\hat{l}}_{eff}(r,\nu)$ describes the effective spatial distribution of the $\hat{l}$-oriented electron−hole pairs (dipole approximation) with the energy $h\nu$ and is normalized such that $\sum_{\hat{l}=\hat{x},\hat{y},\hat{z}} \iiint_{V_m} \phi^{\hat{l}}_{eff}(r,\nu) d^3r = 1$. $\phi^{\hat{l}}_{eff}(r,\nu)$ is a function of the hot carrier energy and spatial distributions throughout the emission, which can evolve as the hot carriers recombine or quasi-ballistically transport and scatter through the metallic parts.[55,56] However, initial distributions of the generated hot carriers highly depend on the excitation conditions, and hence, $\phi^{\hat{l}}_{eff}(r,\nu)$ (and thus L_{eff} (ν)) is also a function of the excitation conditions. In particular, λ_{inc} variation can modify the hot carrier energy distributions by affecting $h\nu_{inc}$ and the factor M_{inc} (Figure 5d inset). Furthermore, by affecting the excitation ratio of the plasmonic modes active at different hot spots, λ_{inc} variation can modify the spatial absorption profile and, thus, the spatial distribution of the hot carriers.[55]

By studying the incident polarization effects, we can better understand the significance of the hot carrier spatial distribution in the nonlinear emission process. Figure 6a displays the H3 nonlinear emission spectra for pol_{inc} = P,S incident polarizations when the incident wavelength and fluence are fixed at λ_{inc} = 1020 nm and E_{inc} = 102 nJ/cm^2, respectively. We see that SHG and ASPL emissions are both higher for pol_{inc} = S. Also, the ASPL intensity ratio $R(\lambda) = S(pol_{inc} = S,\lambda)/S(pol_{inc} = P,\lambda)$, is not uniform and exhibits multiple resonances across the emission band (Figure 6b). The incident polarization has a negligible effect on $\psi_{IBR}(\nu)$ since the incident photon energy $h\nu_{inc}$ is constant and pol_{inc} barely affects the excitation strength factor M_{inc} (Figure 5d inset and Figure S8). Hence, higher nonlinear emission intensity for pol_{inc} = S and $R(\lambda)$ resonances must stem from the pol_{inc}-dependency of $L_{eff}(\nu)$ due to the alteration of the hot carrier spatial distribution.

As depicted in Figure 6a, the S and P incident polarizations yield similar ASPL emission spectral lineshapes. However, placing an analyzer on the emission path shows that the ASPL emission is approximately five times more uniformly distributed across different polarization angles for pol_{inc} = S than pol_{inc} = P (Figure 6c and SI, Figure S9). This observation suggests that the emitted free-space ASPL photons predominantly originate from radiative surface plasmon decay rather than radiative carrier recombination, for three reasons: (i) The electron−hole pairs are randomly oriented, and as a result, ASPL emission generated via radiative electron−hole pair recombination would be unpolarized regardless of the incident polarization, in contrast to the experimental observations. (ii) Our FDTD-based spectral line shape analysis demonstrated that the ASPL emission is dominated by dipole-like z-oriented electron−hole pairs that cannot directly emit along the z-direction to the far field. (iii) Residing inside the metal, electron−hole pairs predominantly interact with the plasmonic optical states rather than the free-space optical states. Therefore, according to the second quantization picture of emission, recombining electron−hole pairs have a low probability of directly emitting free-space photons.[54] Instead of directly generating far-field ASPL photons, electron−hole pairs act as microscopic dipole sources with $\phi^{\hat{l}}_{eff}(r,\nu)$ distribution (eq 5) that can excite the plasmonic modes at the ASPL emission wavelengths (Figure 1d). The excited plasmonic modes then convert a portion of their received energy to the ASPL photons traveling to the far field, while the remaining energy gets reabsorbed by the metal.

To include the surface plasmon mediation process into eq 5, we use the black-box coupled-mode theory[57] to express $F_{\hat{l}}(r,\nu)$ as a summation of the contributions from different plasmonic modes (SI, Section 4):

$$F_{\hat{l}}(r,\nu) = \frac{\gamma_r}{\gamma_r^0} = \sum_p \mathcal{P}_p(\hat{l},r,\nu)\eta_p \quad (6)$$

where γ_r and $\gamma_r^0 = \frac{4\nu^2}{c^3}$ are the radiative decay rates of the dipole in the plasmonic system and the free space, respectively. $\mathcal{P}_p(\hat{l},r,\nu) = \left[\frac{3\epsilon_0 c^3}{(8\pi^2\nu^2)}\right]\sigma_p(\nu)|E_p(r).\hat{l}|^2$ represents the Purcell factor of the p^{th} plasmonic mode, where $E_p(r)$ is the mode normalized electric field and $\sigma_p(\nu) = \frac{\Gamma_p/\pi}{(2\pi\nu - 2\pi\nu_p)^2 + \Gamma_p^2}$ is the

https://doi.org/10.1021/acsnano.3c00559
ACS Nano XXXX, XXX, XXX−XXX

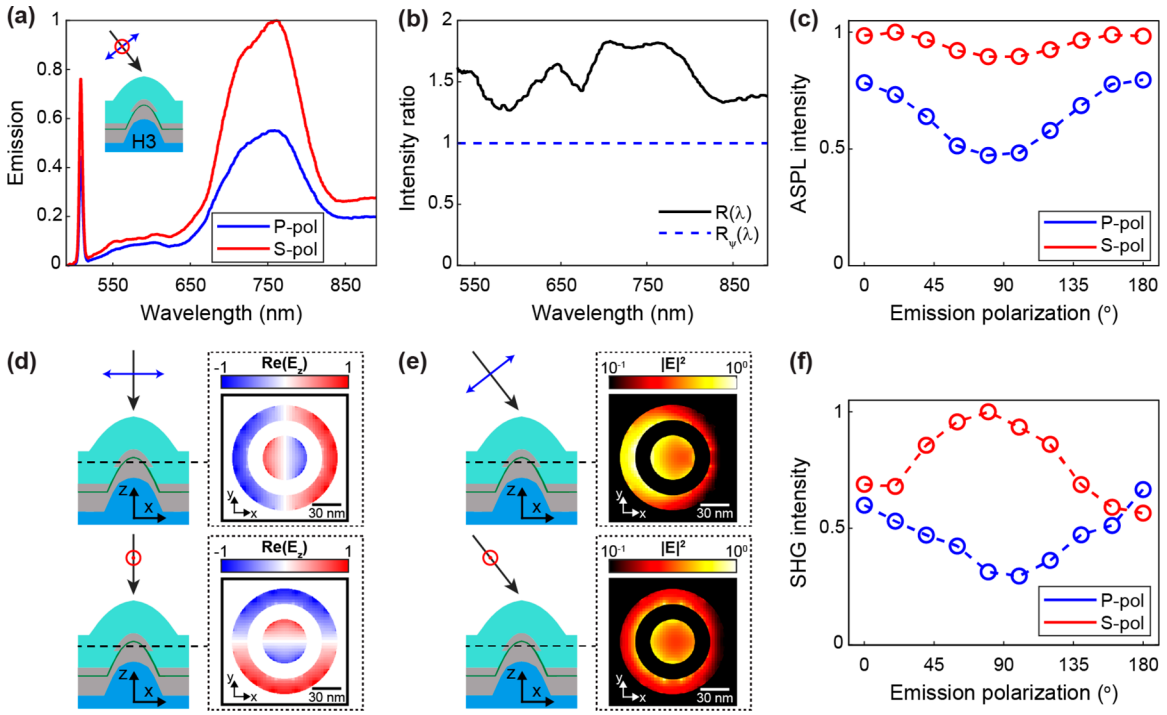

Figure 6. Dependency of SHG and ASPL emissions on the excitation polarization. (a) Our measured upconversion emission spectra $S(pol_{inc},\lambda)$ of the H3 sample upon ultrashort pulsed laser excitation (λ_{inc} = 1020 nm, and E_{inc} = 204 nJ/cm^2) with pol_{inc} = *P* and pol_{inc} = *S* incident polarizations. (b) The ratiometric ASPL spectra, $R(\lambda) = S(pol_{inc} = S,\lambda)/S(pol_{inc} = P,\lambda)$, from the measurements in Figure 6a, and $R_\psi(\lambda)$, the ratiometric ASPL spectra when only the effect of pol_{inc} on the modification of the electron energy distribution is considered. (c) The observed ASPL intensity I_{ASPL} (530−890 nm) as a function of the emission polarization angle for each of the P and S incident polarizations. (d) FDTD-calculated $Re(E_z)$ distributions at 761 nm for the H3 sample under normal excitation with P and S incident polarizations. The dashed lines in the schematics represent the field monitor planes. The $Re(E_z)$ profiles manifest the presence of degenerate plasmonic modes with perpendicular polarizations. (e) FDTD-calculated $|E|^2$ distributions at 1020 nm for the H3 sample under 30°-angled excitation with P and S incident polarizations. $|E|^2$ profiles at the excitation wavelength determine the spatial distribution of the hot carriers right after their generation. (f) The observed SHG intensity I_{SHG} (505−515 nm) as a function of the emission polarization angle for each of the P and S incident polarizations.

mode spectral line shape. ν_p is the mode resonance frequency and $\Gamma_p = \Gamma^r_p + \Gamma^{nr}_p$ is the mode decay rate, with Γ^r_p and Γ^{nr}_p being the radiative and nonradiative components. Also, $\eta_p = \Gamma^r_p/\Gamma_p$ is the quantum efficiency of the p^{th} plasmonic mode for radiative coupling to the far field. By combining eqs 2−3 and 5−6, we can rewrite the ASPL spectral intensity formula as

$$S_{ASPL}(\nu) \propto f_{inc} \sum_p \gamma_p^{ASPL}(\nu)\eta_p \tag{7}$$

where $\gamma_p^{ASPL}(\nu) \propto (h\nu)\psi_{IBR}(\nu)\sigma_p(\nu)\sum_{\hat{l}=\hat{x}\hat{y}\hat{z}}\iiint_{V_m}\phi^l_{eff}(r,\nu)\,|E_p(r).\hat{l}|^2 d^3r$ represents the level of energy transfer from the hot carriers to the p^{th} plasmonic mode at the frequency ν. eq 7 shows that the contribution level of the p^{th} plasmonic mode to the PL emission depends on: (i) $\psi_{IBR}(\nu)\sigma_p(\nu)$, i.e., the spectral overlap between the hot electron−hole pairs and the plasmonic mode, (ii) $\iiint_{V_m}\phi^l_{eff}(r,\nu)|E_p(r).\hat{l}|^2 d^3r$, i.e., the spatial overlap between the hot electron−hole pairs and the plasmonic field, and (iii) the plasmonic mode quantum efficiency η_p.

Due to structural symmetry, nanolaminate plasmonic crystals support two sets of degenerate plasmonic modes with perpendicular polarizations (Figure 6d and SI, Figure S10). As per eq 7, the amount of the ASPL emission mediated by each set depends on the extent of its spatial overlap with the hot electron−hole pair distribution $\phi^l_{eff}(r,\nu)$. Spatial distribution of $\phi^l_{eff}(r,\nu)$ is contingent on the initial spatial distribution of the hot carriers, which follows the excitation intensity profile ($|E_{ex}|^2$) within the metallic components.[55] Our FDTD simulations show that $|E_{ex}|^2$ profile, and hence $\phi^l_{eff}(r,\nu)$ spatial distribution, are more uniform for $pol_{inc} = S$ than for $pol_{inc} = P$ (Figure 6e), leading to a more balanced contribution of the two sets of perpendicular degenerate plasmonic modes to the ASPL emission for $pol_{inc} = S$. As a result, switching pol_{inc} from P to S yields a more uniform angular distribution of the emission polarization with minor alterations to the ASPL line shape, consistent with the experimental observations in Figures 6a and 6c. The more uniform $|E_{ex}|^2$ profile under $pol_{inc} = S$ can also cause its higher ASPL emission intensity observed in Figure 6a (see more details in SI, Section 4). While our FDTD-based analysis reasonably captures the trends observed in the excitation and emission polarization measurements, it cannot precisely reproduce the experimentally observed angular distributions of the ASPL emission polarization (Figure 6c). A more comprehensive analysis necessitates considering the nonidealities, such as structural defects and surface roughness, which can modify the plasmonic field distributions and act as scattering or trapping centers for the hot carriers.

Figure 6f shows the angular distribution of the SHG emission polarization for the S and P incident polarizations. Like ASPL, the nonuniformity observed in the SHG emission polarization and its dependence on pol_{inc} manifests that the emitted SHG photons come from the radiative decay of the second-harmonic-excited surface plasmons (Figure 1f) rather than direct emission of the microscopic SHG dipole sources at the metal surface to the free space. However, unlike the observed ASPL responses in Figure 6c, SHG intensity becomes the highest when the

https://doi.org/10.1021/acsnano.3c00559
ACS Nano XXXX, XXX, XXX−XXX

excitation and emission polarizations are aligned, manifesting the coherence between the excitation and SHG photons.

Since NLPCs consist of centrosymmetric materials, bulk second-order susceptibility $\chi^{(2)}$ is negligible, and SHG mainly arises from the metallic interfaces with broken centrosymmetry and high plasmon-enhanced optical field intensity.[7] We can use the black-box coupled-mode theory[57] to express the SHG emission intensity as a summation of emission intensities from individual plasmonic modes (SI, section 5):

$$S_{SHG}(2\nu_{inc}) \propto f_{inc} \sum_{p} \gamma_p^{SHG}(2\nu_{inc})\eta_p \tag{8}$$

where $\gamma_p^{SHG}(2\nu_{inc}) \propto (\nu_{inc})^2\sigma_p(2\nu_{inc})\int_{-\infty}^{+\infty}|\int\int_{\partial_m}\chi^{(2)}(t)(E_{ex}(t).\hat{n})^2(E_p.\hat{n})^* dS|^2 dt$, with ∂_m and $\hat{n}$ representing the metallic surfaces and their normal vectors, respectively. Since SHG is a coherent process, the phase information for E_{ex} and E_p electric field components is essential in the γ_p^{SHG} formulation, in contrast with the γ_p^{ASPL} formulation in eq 7. Time-dependency of $\chi^{(2)}$ in γ_p^{SHG} formula reflects that perturbation of the electron distribution by the intense excitation electric fields can modulate $\chi^{(2)}$ in the time domain. For high incident intensities, $\chi^{(2)}$ becomes E_{inc}-dependent, leading to >2 power-law exponents for SHG, as experimentally observed in Figure 3d.

eq 8 suggests that (SI, section 5), irrespective of the incident polarization, SHG should ideally be x-polarized (polarization angle = 0) since the angled incident beam only breaks the symmetry in the x-direction (SI, Figure S11). However, experimental observations deviate from this theoretical prediction (Figure 6f), implying that surface imperfections in the fabricated NLPC samples can disrupt the geometrical symmetry and randomize the E_{ex} and E_p phases, thereby preventing the completely destructive interference of the microscopic SHG sources for y-polarized emission (polarization angle = 90°).

CONCLUSIONS

In conclusion, we have demonstrated dual-modal plasmon-enhanced light upconversion through ASPL and SHG from broadband multiresonant metal nanocavities in two-tier NLPCs. Our combined experimental and theoretical study investigates the differences and correlations between the plasmon-enhanced ASPL and SHG processes under various ultrashort pulsed laser excitation conditions, including incident fluence, wavelength, and polarization. We developed a robust time-domain modeling framework to understand the observed influences of optical excitation and modal conditions on ASPL and SHG emissions. This framework captures the mode coupling-enhancement characteristics, quantum excitation−emission transitions, and hot carrier population statistical mechanics. Notably, our ASPL model considers (i) both IBR and ERS pathways, (ii) time-evolved hot carrier energy distributions with electron-photon, electron−electron, and electron−phonon interactions, and (iii) momentum conservation in electronic excitation and emission transitions. Our study reveals that the IBR pathway dominates the ASPL emission from NLPCs under ultrashort pulsed laser excitation. We found that the excitation strength as a function of the incident laser fluence and plasmonic enhancement level at the excitation wavelength can significantly influence the temporal, spectral, and power-law characteristics of the ASPL emission through controlling the contribution ratios of the native, excess nonthermalized, and excess thermalized carriers. Furthermore, our study shows that ASPL and SHG photons both originate from radiative surface plasmon annihilation but exhibit different emission behaviors due to the intrinsic difference between instantaneous SHG sources at the metal surface and the incoherent hot carrier-mediated ASPL emitters that feature a temporally evolving energy and spatial distribution. Further investigation is needed to examine the dependence of ASPL and SHG processes on plasmonic metal types (e.g., Ag, Au, Cu, Al) both with and without interband photoluminescence pathways. Nevertheless, our findings represent a significant step toward understanding and applying ASPL and SHG upconversion in broadband multiresonant metallic nanocavities for multimodal or wavelength-multiplexed operations in bioimaging, sensing, interfacial monitoring, and integrated photonics.

METHODS AND EXPERIMENTAL

Numerical Calculations. We performed three-dimensional Finite Difference Time Domain simulations using the software ANSYS-Lumerical FDTD solutions to numerically calculate the far-field spectra and the near-field distributions for the plasmonic crystals. We used a uniform mesh size of 3 nm with periodic boundary conditions in the x and y directions and PML boundaries in the z direction. The silver dielectric function was obtained from the Palik handbook of optical constants for solids.[58] Also, the constant refractive index of 1.5 was used for SiO_2.

Absorption Measurements. We used Cary 5000 spectrophotometer to measure the reflectance (R) spectra with a monochromator and integrating sphere setup. As the samples have zero transmission ($T = 0$), we obtained the absorption (A) spectra from the equation: $A = 1 - R$.

Nonlinear Emission Measurements. As shown in Figure 1c, we exploited a wavelength-tunable Ti: Sapphire laser module (Chameleon Ultra II) to generate ultrashort laser excitation pulses with the duration of Δt_{inc} = 140 fs and the repetition rate of f_{inc} = 80 MHz. We used an acousto-optic modulator to attenuate the laser pulses and control the irradiance power incident on the sample. The laser incidence angle was 30°, and its polarization was controlled using a half-wave plate. We adjusted a set of beam-shaping lenses to get a ∼1 mm laser spot size on the samples and utilized a NA = 0.1 collimating lens to collect the nonlinear emission signals from samples in the normal direction. After going through a set of filters (490−900 nm) to block the excitation background signal, the collected emission signals were spectrally analyzed by a nitrogen-cooled CCD spectrometer (Horiba iHR550). We also placed an analyzer on the emission beam path to measure the nonlinear emission spectra at different emission polarization. All the measurements were conducted at the room temperature T_0 = 300 K.

ASSOCIATED CONTENT

Supporting Information

The Supporting Information is available free of charge at https://pubs.acs.org/doi/10.1021/acsnano.3c00559.

Methods for power-law exponent calculations, hot carrier energy distribution modeling, photoluminescence modeling, PL emission enhancement modeling, and second harmonic generation modeling (PDF)

AUTHOR INFORMATION

Corresponding Authors

Wei Zhou − *Department of Electrical and Computer Engineering, Virginia Tech, Blacksburg, Virginia 24061, United States;* orcid.org/0000-0002-5257-3885; Email: wzh@vt.edu

https://doi.org/10.1021/acsnano.3c00559
ACS Nano XXXX, XXX, XXX−XXX

Giti A. Khodaparast − *Department of Physics, Virginia Tech, Blacksburg, Virginia 24061, United States*; Email: khoda@vt.edu

Authors

Seied Ali Safiabadi Tali − *Department of Electrical and Computer Engineering, Virginia Tech, Blacksburg, Virginia 24061, United States*; orcid.org/0000-0002-6195-9640

Rathsara R. H. H. Mudiyanselage − *Department of Physics, Virginia Tech, Blacksburg, Virginia 24061, United States*

Yizhou Qian − *Department of Electrical and Computer Engineering, Virginia Tech, Blacksburg, Virginia 24061, United States*; orcid.org/0000-0002-2157-0497

Nicholas William Gary Smith − *Department of Physics, Virginia Tech, Blacksburg, Virginia 24061, United States*

Yuming Zhao − *Department of Electrical and Computer Engineering, Virginia Tech, Blacksburg, Virginia 24061, United States*

Ada Morral − *Department of Physics, Virginia Tech, Blacksburg, Virginia 24061, United States*; orcid.org/0000-0002-1366-8136

Junyeob Song − *Department of Electrical and Computer Engineering, Virginia Tech, Blacksburg, Virginia 24061, United States*; orcid.org/0000-0001-6369-823X

Meitong Nie − *Department of Electrical and Computer Engineering, Virginia Tech, Blacksburg, Virginia 24061, United States*

Brenden A. Magill − *Department of Physics, Virginia Tech, Blacksburg, Virginia 24061, United States*

Complete contact information is available at: https://pubs.acs.org/10.1021/acsnano.3c00559

Author Contributions

[§]S.T.S.A. and R.R.H.H.M. share equal contributions. S.T.S.A. and W.Z. conceived the idea. W. Z. and G.A.K. supervised the project. S.T.S.A. performed plasmonic sample design and fabrication, linear optical measurements, numerical simulations, and the corresponding data analysis with the help of W.Z., Y.Q., Y.Z., J.S., and M.N. R.R.H.H.M. performed nonlinear upconversion emission measurements and related data analysis with the help of N.W.G.S., A.M., B.A.M., and G.A.K. J.S. contributed to structural characterization by FIB/SEM. S.T.S.A. and W.Z. wrote the manuscript with the contributions of all authors. All authors have approved the final version of the manuscript.

Notes

The authors declare no competing financial interest.

ACKNOWLEDGMENTS

W.Z. acknowledges the support of the AFOSR Young Investigator Award (FA9550-18-1-0328), AFOSR DURIP grant (FA9550-19-1-0287), NIST grant (70NANB18H201), and NSF grant (DMR 2139317). G.A.K. acknowledges the support of the AFOSR grant (FA9550-17-1-0341) and DURIP funding (FA9550-16-1-0358). G.A.K. and R.R.H.H.M. acknowledge the support from L.C. Hassinger Faculty Fellowship. A.M. acknowledges the partial support from Clare Boothe Luce Program at Virginia Tech.

REFERENCES

(1) Pelton, M. Modified spontaneous emission in nanophotonic structures. *Nat. Photonics* **2015**, *9* (7), 427−435.

(2) Sun, G.; Khurgin, J. B. Origin of giant difference between fluorescence, resonance, and nonresonance Raman scattering enhancement by surface plasmons. *Phys. Rev. A* **2012**, *85* (6), 063410.

(3) Kauranen, M.; Zayats, A. V. Nonlinear plasmonics. *Nat. Photonics* **2012**, *6* (11), 737−748.

(4) Kinkhabwala, A.; Yu, Z. F.; Fan, S. H.; Avlasevich, Y.; Mullen, K.; Moerner, W. E. Large single-molecule fluorescence enhancements produced by a bowtie nanoantenna. *Nat. Photonics* **2009**, *3* (11), 654−657.

(5) Zhou, W.; Dridi, M.; Suh, J. Y.; Kim, C. H.; Co, D. T.; Wasielewski, M. R.; Schatz, G. C.; Odom, T. W. Lasing action in strongly coupled plasmonic nanocavity arrays. *Nat. Nanotechnol.* **2013**, *8* (7), 506−511.

(6) Aouani, H.; Rahmani, M.; Navarro-Cia, M.; Maier, S. A. Third-harmonic-upconversion enhancement from a single semiconductor nanoparticle coupled to a plasmonic antenna. *Nat. Nanotechnol.* **2014**, *9* (4), 290−294.

(7) Krasnok, A.; Tymchenko, M.; Alu, A. Nonlinear metasurfaces: a paradigm shift in nonlinear optics. *Mater. Today* **2018**, *21* (1), 8−21.

(8) Celebrano, M.; Wu, X. F.; Baselli, M.; Grossmann, S.; Biagioni, P.; Locatelli, A.; De Angelis, C.; Cerullo, G.; Osellame, R.; Hecht, B.; Duo, L.; Ciccacci, F.; Finazzi, M. Mode matching in multiresonant plasmonic nanoantennas for enhanced second harmonic generation. *Nat. Nanotechnol.* **2015**, *10* (5), 412−417.

(9) Kim, S.; Jin, J. H.; Kim, Y. J.; Park, I. Y.; Kim, Y.; Kim, S. W. High-harmonic generation by resonant plasmon field enhancement. *Nature* **2008**, *453* (7196), 757−760.

(10) Shen, Q. X.; Jin, W. L.; Yang, G.; Rodriguez, A. W.; Mikkelsen, M. H. Active Control of Multiple, Simultaneous Nonlinear Optical Processes in Plasmonic Nanogap Cavities. *Acs Photonics* **2020**, *7* (4), 901−907.

(11) Krauth, J.; Giessen, H.; Hentschel, M. Wavelength-Dependent Third-Harmonic Generation in Plasmonic Gold Nanoantennas: Quantitative Determination of the d-Band Influence. *Acs Photonics* **2018**, *5* (5), 1863−1870.

(12) Dass, C. K.; Kwon, H.; Vangala, S.; Smith, E. M.; Cleary, J. W.; Guo, J.; Alu, A.; Hendrickson, J. R. Gap-Plasmon-Enhanced Second-Harmonic Generation in Epsilon-Near-Zero Nanolayers. *Acs Photonics* **2020**, *7* (1), 174−179.

(13) Krasavin, A. V.; Ginzburg, P.; Wurtz, G. A.; Zayats, A. V. Nonlocality-driven supercontinuum white light generation in plasmonic nanostructures. *Nat. Commun.* **2016**, *7*, 11497.

(14) Cai, Y. Y.; Tauzin, L. J.; Ostovar, B.; Lee, S.; Link, S. Light emission from plasmonic nanostructures. *J. Chem. Phys.* **2021**, *155* (6), 060901.

(15) Cai, Y. Y.; Sung, E.; Zhang, R.; Tauzin, L. J.; Liu, J. G.; Ostovar, B.; Zhang, Y.; Chang, W. S.; Nordlander, P.; Link, S. Anti-Stokes Emission from Hot Carriers in Gold Nanorods. *Nano Lett.* **2019**, *19* (2), 1067−1073.

(16) Roloff, L.; Klemm, P.; Gronwald, I.; Huber, R.; Lupton, J. M.; Bange, S. Light Emission from Gold Nanoparticles under Ultrafast Near-Infrared Excitation: Thermal Radiation, Inelastic Light Scattering, or Multiphoton Luminescence. *Nano Lett.* **2017**, *17* (12), 7914−7919.

(17) Haug, T.; Klemm, P.; Bange, S.; Lupton, J. M. Hot-Electron Intraband Luminescence from Single Hot Spots in Noble-Metal Nanoparticle Films. *Phys. Rev. Lett.* **2015**, *115* (6), 067403.

(18) Carles, R.; Bayle, M.; Benzo, P.; Benassayag, G.; Bonafos, C.; Cacciato, G.; Privitera, V. Plasmon-resonant Raman spectroscopy in metallic nanoparticles: Surface-enhanced scattering by electronic excitations. *Phys. Rev. B* **2015**, *92* (17), 174302.

(19) Huang, J.; Wang, W.; Murphy, C. J.; Cahill, D. G. Resonant secondary light emission from plasmonic Au nanostructures at high electron temperatures created by pulsed-laser excitation. *Proc. Natl. Acad. Sci. U. S. A.* **2014**, *111* (3), 906−911.

(20) Mesch, M.; Metzger, B.; Hentschel, M.; Giessen, H. Nonlinear Plasmonic Sensing. *Nano Lett.* **2016**, *16* (5), 3155−3159.

(21) Bonacina, L. Nonlinear Nanomedecine: Harmonic Nanoparticles toward Targeted Diagnosis and Therapy. *Mol. Pharmaceut* **2013**, *10* (3), 783−792.

(22) Valev, V. K. Characterization of Nanostructured Plasmonic Surfaces with Second Harmonic Generation. *Langmuir* **2012**, *28* (44), 15454−15471.
(23) Butet, J.; Russier-Antoine, I.; Jonin, C.; Lascoux, N.; Benichou, E.; Brevet, P. F. Sensing with Multipolar Second Harmonic Generation from Spherical Metallic Nanoparticles. *Nano Lett.* **2012**, *12* (3), 1697−1701.
(24) Ray, P. C. Size and Shape Dependent Second Order Nonlinear Optical Properties of Nanomaterials and Their Application in Biological and Chemical Sensing. *Chem. Rev.* **2010**, *110* (9), 5332−5365.
(25) Wang, C.; Li, Z. Y.; Kim, M. H.; Xiong, X.; Ren, X. F.; Guo, G. C.; Yu, N. F.; Loncar, M. Metasurface-assisted phase-matching-free second harmonic generation in lithium niobate waveguides. *Nat. Commun.* **2017**, *8*, 2098.
(26) Sivan, Y.; Dubi, Y. Theory of "Hot" Photoluminescence from Drude Metals. *ACS Nano* **2021**, *15* (5), 8724−8732.
(27) Carattino, A.; Caldarola, M.; Orrit, M. Gold Nanoparticles as Absolute Nanothermometers. *Nano Lett.* **2018**, *18* (2), 874−880.
(28) Xie, X.; Cahill, D. G. Thermometry of plasmonic nanostructures by anti-Stokes electronic Raman scattering. *Appl. Phys. Lett.* **2016**, *109* (18), 183104.
(29) Zheng, Z. K.; Tachikawa, T.; Majima, T. Single-Particle Study of Pt-Modified Au Nanorods for Plasmon-Enhanced Hydrogen Generation in Visible to Near-Infrared Region. *J. Am. Chem. Soc.* **2014**, *136* (19), 6870−6873.
(30) Durr, N. J.; Larson, T.; Smith, D. K.; Korgel, B. A.; Sokolov, K.; Ben-Yakar, A. Two-photon luminescence imaging of cancer cells using molecularly targeted gold nanorods. *Nano Lett.* **2007**, *7* (4), 941−945.
(31) Zheng, Z. K.; Majima, T. Nanoplasmonic Photoluminescence Spectroscopy at Single-Particle Level: Sensing for Ethanol Oxidation. *Angew. Chem. Int. Edit* **2016**, *55* (8), 2879−2883.
(32) Boyd, G. T.; Yu, Z. H.; Shen, Y. R. Photoinduced Luminescence from the Noble-Metals and Its Enhancement on Roughened Surfaces. *Phys. Rev. B* **1986**, *33* (12), 7923−7936.
(33) Mooradian, A. Photoluminescence of Metals. *Phys. Rev. Lett.* **1969**, *22* (5), 185.
(34) Beversluis, M. R.; Bouhelier, A.; Novotny, L. Continuum generation from single gold nanostructures through near-field mediated intraband transitions. *Phys. Rev. B* **2003**, *68* (11), 115433.
(35) Ostovar, B.; Cai, Y. Y.; Tauzin, L. J.; Lee, S. A.; Ahmadivand, A.; Zhang, R.; Nordlander, P.; Link, S. Increased Intraband Transitions in Smaller Gold Nanorods Enhance Light Emission. *ACS Nano* **2020**, *14* (11), 15757−15765.
(36) Cai, Y. Y.; Liu, J. G.; Tauzin, L. J.; Huang, D.; Sung, E.; Zhang, H.; Joplin, A.; Chang, W. S.; Nordlander, P.; Link, S. Photoluminescence of Gold Nanorods: Purcell Effect Enhanced Emission from Hot Carriers. *ACS Nano* **2018**, *12* (2), 976−985.
(37) Lin, K.-Q.; Yi, J.; Hu, S.; Sun, J.-J.; Zheng, J.-T.; Wang, X.; Ren, B. Intraband hot-electron photoluminescence from single silver nanorods. *Acs Photonics* **2016**, *3* (7), 1248−1255.
(38) Mertens, J.; Kleemann, M. E.; Chikkaraddy, R.; Narang, P.; Baumberg, J. J. How Light Is Emitted by Plasmonic Metals. *Nano Lett.* **2017**, *17* (4), 2568−2574.
(39) Hugall, J. T.; Baumberg, J. J. Demonstrating Photoluminescence from Au is Electronic Inelastic Light Scattering of a Plasmonic Metal: The Origin of SERS Backgrounds. *Nano Lett.* **2015**, *15* (4), 2600−2604.
(40) Nam, W.; Zhao, Y. M.; Song, J.; Safiabadi Tali, S. A.; Kang, S. J.; Zhu, W. Q.; Lezec, H. J.; Agrawal, A.; Vikesland, P. J.; Zhou, W. Plasmonic Electronic Raman Scattering as Internal Standard for Spatial and Temporal Calibration in Quantitative Surface-Enhanced Raman Spectroscopy. *J. Phys. Chem. Lett.* **2020**, *11* (22), 9543−9551.
(41) Yorulmaz, M.; Khatua, S.; Zijlstra, P.; Gaiduk, A.; Orrit, M. Luminescence quantum yield of single gold nanorods. *Nano Lett.* **2012**, *12* (8), 4385−4391.
(42) Mohamed, M. B.; Volkov, V.; Link, S.; El-Sayed, M. A. Thelightning'gold nanorods: fluorescence enhancement of over a million compared to the gold metal. *Chem. Phys. Lett.* **2000**, *317* (6), 517−523.
(43) Dulkeith, E.; Niedereichholz, T.; Klar, T.; Feldmann, J.; Von Plessen, G.; Gittins, D.; Mayya, K.; Caruso, F. Plasmon emission in photoexcited gold nanoparticles. *Phys. Rev. B* **2004**, *70* (20), 205424.
(44) Bouhelier, A.; Bachelot, R.; Lerondel, G.; Kostcheev, S.; Royer, P.; Wiederrecht, G. Surface plasmon characteristics of tunable photoluminescence in single gold nanorods. *Physical review letters* **2005**, *95* (26), 267405.
(45) Tcherniak, A.; Dominguez-Medina, S.; Chang, W.-S.; Swanglap, P.; Slaughter, L. S.; Landes, C. F.; Link, S. One-photon plasmon luminescence and its application to correlation spectroscopy as a probe for rotational and translational dynamics of gold nanorods. *J. Phys. Chem. C* **2011**, *115* (32), 15938−15949.
(46) Safiabadi Tali, S. A.; Song, J.; Nam, W.; Zhou, W. Two-Tier Nanolaminate Plasmonic Crystals for Broadband Multiresonant Light Concentration with Spatial Mode Overlap. *Advanced Optical Materials* **2021**, *9* (10), 2001908.
(47) Safiabadi Tali, S. A.; Song, J.; Nam, W.; Zhou, W. Two-Tier Nanolaminate Plasmonic Crystals for Broadband Multiresonant Light Concentration with Spatial Mode Overlap. *Advanced Optical Materials* **2021**, *9* (10), 2001908.
(48) Boyd, R. W. *Nonlinear optics*; Academic Press: Cambridge, 2020.
(49) Borys, N. J.; Walter, M. J.; Lupton, J. M. Intermittency in second-harmonic radiation from plasmonic hot spots on rough silver films. *Phys. Rev. B* **2009**, *80* (16), 161407.
(50) Khurgin, J. B. How to deal with the loss in plasmonics and metamaterials. *Nat. Nanotechnol.* **2015**, *10* (1), 2−6.
(51) Voisin, C.; Christofilos, D.; Loukakos, P. A.; Del Fatti, N.; Vallee, F.; Lerme, J.; Gaudry, M.; Cottancin, E.; Pellarin, M.; Broyer, M. Ultrafast electron-electron scattering and energy exchanges in noble-metal nanoparticles. *Phys. Rev. B* **2004**, *69* (19), 195416.
(52) Del Fatti, N.; Voisin, C.; Achermann, M.; Tzortzakis, S.; Christofilos, D.; Vallee, F. Nonequilibrium electron dynamics in noble metals. *Phys. Rev. B* **2000**, *61* (24), 16956−16966.
(53) Sun, C. K.; Vallee, F.; Acioli, L. H.; Ippen, E. P.; Fujimoto, J. G. Femtosecond-Tunable Measurement of Electron Thermalization in Gold. *Phys. Rev. B* **1994**, *50* (20), 15337−15348.
(54) Novotny, L.; Hecht, B. *Principles of nano-optics*; Cambridge University Press: Cambridge, U.K., 2012.
(55) Cortes, E.; Xie, W.; Cambiasso, J.; Jermyn, A. S.; Sundararaman, R.; Narang, P.; Schlucker, S.; Maier, S. A. Plasmonic hot electron transport drives nano-localized chemistry. *Nat. Commun.* **2017**, *8*, 14880.
(56) Brown, A. M.; Sundararaman, R.; Narang, P.; Goddard, W. A.; Atwater, H. A. Nonradiative Plasmon Decay and Hot Carrier Dynamics: Effects of Phonons, Surfaces, and Geometry. *ACS Nano* **2016**, *10* (1), 957−966.
(57) Tali, S. A. S.; Yuan, L.; Zhou, W., Black-Box Coupled-Mode Theory: An Ab Initio Framework to Model Electromagnetic Interactions of Open, Lossy, and Dispersive Resonators. *arXiv*, Nov. 19, 2020, 2011.10035, ver. 1. DOI: 10.48550/arXiv.2011.10035 (accessed May 1, 2023).
(58) Palik, E. D. *Handbook of optical constants of solids*; Academic Press: Cambridge, USA, 1998; Vol. *3*.

https://doi.org/10.1021/acsnano.3c00559
ACS Nano XXXX, XXX, XXX−XXX